Science Advances
◣AAAS

Supplementary Materials for

Interdependence of a mechanosensitive anion channel and glutamate receptors in distal wound signaling

Jacob Moe-Lange, Nicoline M. Gappel, Mackenzie Machado, Michael M. Wudick, Cosima S. A. Sies, Stephan N. Schott-Verdugo, Michele Bonus, Swastik Mishra, Thomas Hartwig, Margaret Bezrutczyk, Debarati Basu, Edward E. Farmer, Holger Gohlke, Andrey Malkovskiy, Elizabeth S. Haswell, Martin J. Lercher, David W. Ehrhardt, Wolf B. Frommer*, Thomas J. Kleist
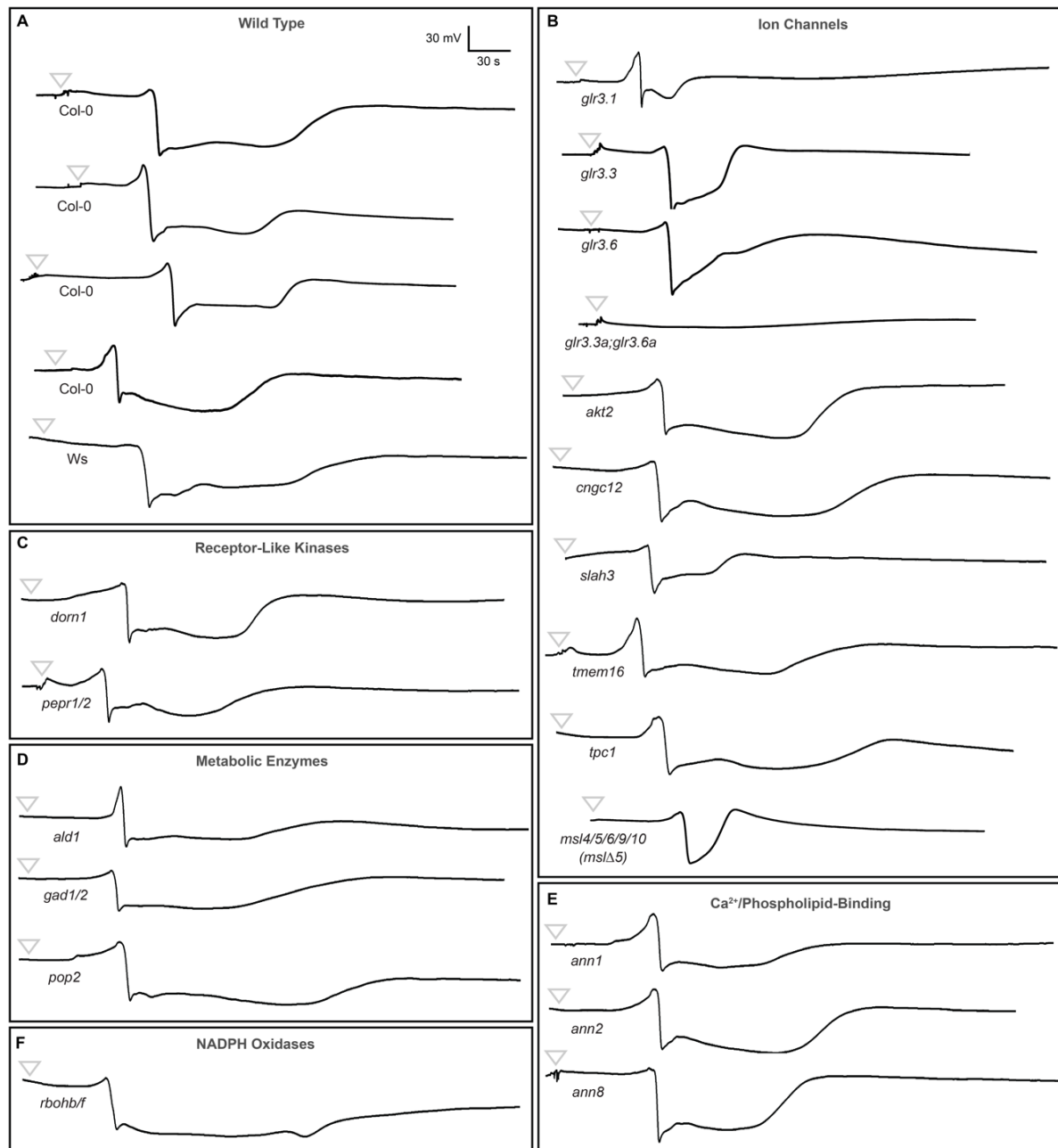
*Corresponding author. Email: frommew@hhu.de

The PDF file includes:

> Figs. S1 to S15
> Tables S1 to S6
> Legends for movies S1 to S6
> References

Other Supplementary Material for this manuscript includes the following:

> Movies S1 to S6
> Data files S1 to S3

Figure S1. SWP recordings in wild type and candidate mutants. Leaf 8 was wounded by mechanical crushing with a pair of modified pliers at the time points indicated by arrowheads. Traces show surface potential recordings of distal parastichous leaf 13. **(A)** Example traces of wild-type SWP recordings in Col-0 and Wassilewskija (Ws) ecotypes. **(B)** Example traces depicting SWP recordings of mutants lacking ion channels associated with membrane depolarizations. **(C)** Example traces depicting SWP recordings of mutants lacking receptor-like kinases implicated in plant defense. **(D)** Example traces depicting SWP recordings of mutants lacking genes involved in glutamate metabolism. **(E)** Example traces depicting SWP recordings of mutants deficient in genes shown to be involved with Ca^{2+} and/or phospholipid-binding and possibly ion transport. **(F)** Example trace depicting a SWP recording of a double mutant deficient in genes involved in ROS production. Abbreviations for candidate mutants and sequences of primers used for genotyping are summarized in Extended Data Table 1. Unless otherwise noted, *n* = 4-6; *n* for Col-0, *glr3.3, glr3.6, mslΔ5, msl10-1, and msl10-2* are given in Table S2.
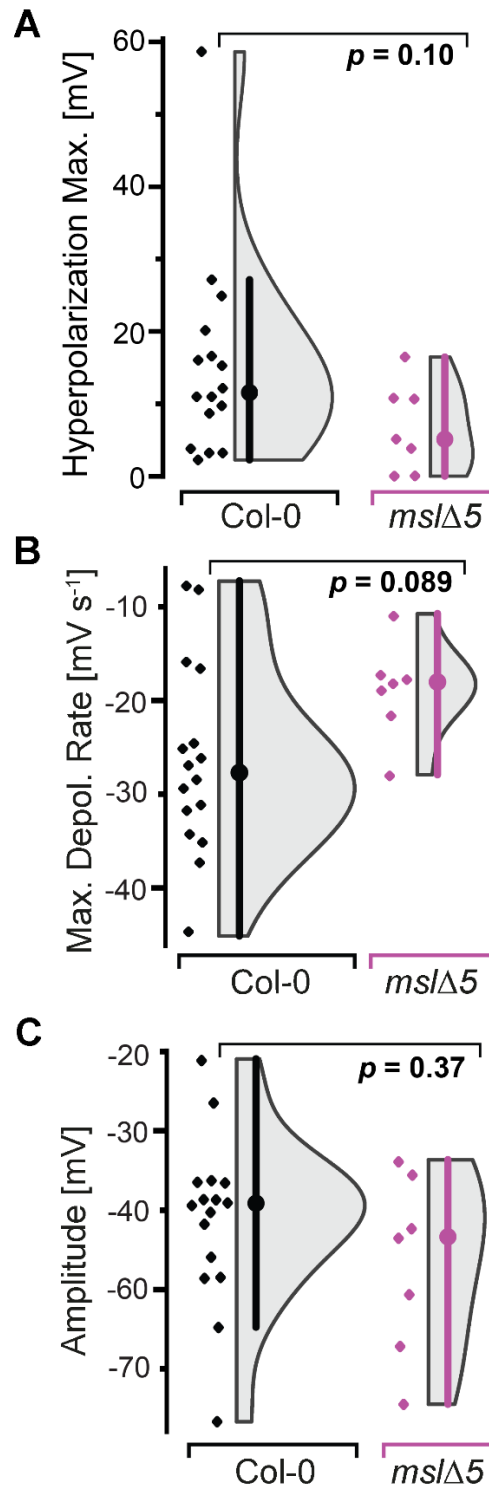
Figure S2. Statistical analysis of *mslΔ5* L13 SWP parameters in comparison to Col-0. (A) SWP hyperpolarization maximum (HM) prior to the depolarization event (median ± S.E.M.: Col-0: 11.6 ± 3.5 mV; *mslΔ5*: 5.1 ± 2.3 mV). **(B)** SWP maximum depolarization rate (median ± S.E.M: Col-0: -27.7 ± 2.5 mV s^{-1}, *mslΔ5*: -18.2 7 ± 1.9 mV s^{-1}). **(C)** SWP amplitudes (median ± S.E.M.: Col-0: -43.9 ± 4.0 mV; *mslΔ5*: -50.3 ± 6.4 mV). Half-violin plots show kernel density estimates (KDEs) calculated using Scott's estimated bandwidth; circle: median; whiskers: 1.5 x IQR; *p*-values generated by Mann-Whitney U test (n = 7-15).
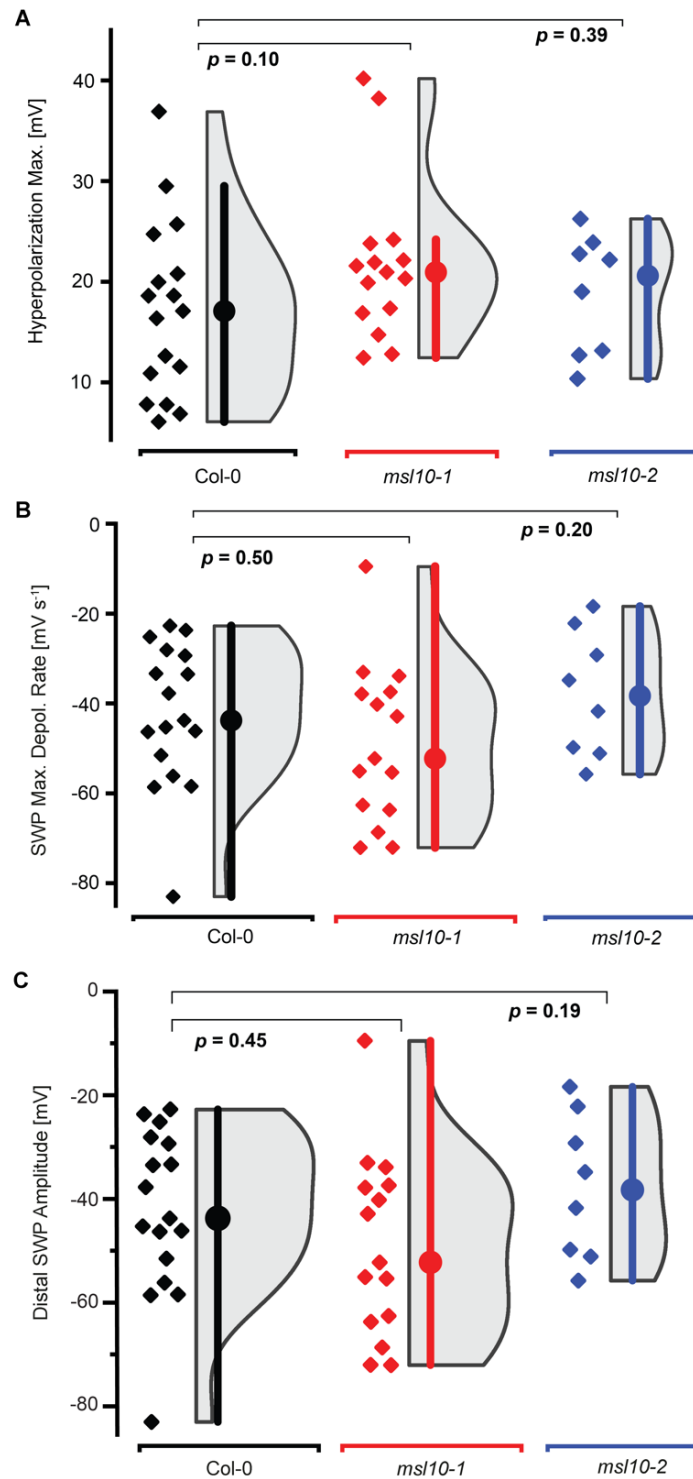
Figure S3. Statistical analysis of *msl10-1* and *msl10-2* L13 SWP parameters in comparison to Col-0. (**A**) SWP hyperpolarization maxima (median ± S.E.M.: Col-0: 17.2 ± 2.1 mV, *msl10-1*: 21.4 ± 2.1 mV, *msl10-2*: 18.8 ± 2.1 mV). (B) SWP maximum depolarization (Max. Depol.) rate (median ± S.E.M.: Col-0: -42.5 ± 3.9 mV, *msl10-1*: -45.1 ± 4.6 mV, *msl10-2*: -37.9 ± 4.9 mV). (**C**) SWP amplitude (median ± S.E.M.: Col-0: -48.1 ± 3.2 mV, *msl10-1*: -59.6 ± 4.7 mV, *msl10-2*: -43.7 ± 4.0 mV). Half-violin plots show kernel density estimates calculated using Scott's estimated bandwidth; circle: median; whiskers: 1.5 x IQR; *p*-values generated by Mann-Whitney U test (n = 8-17).
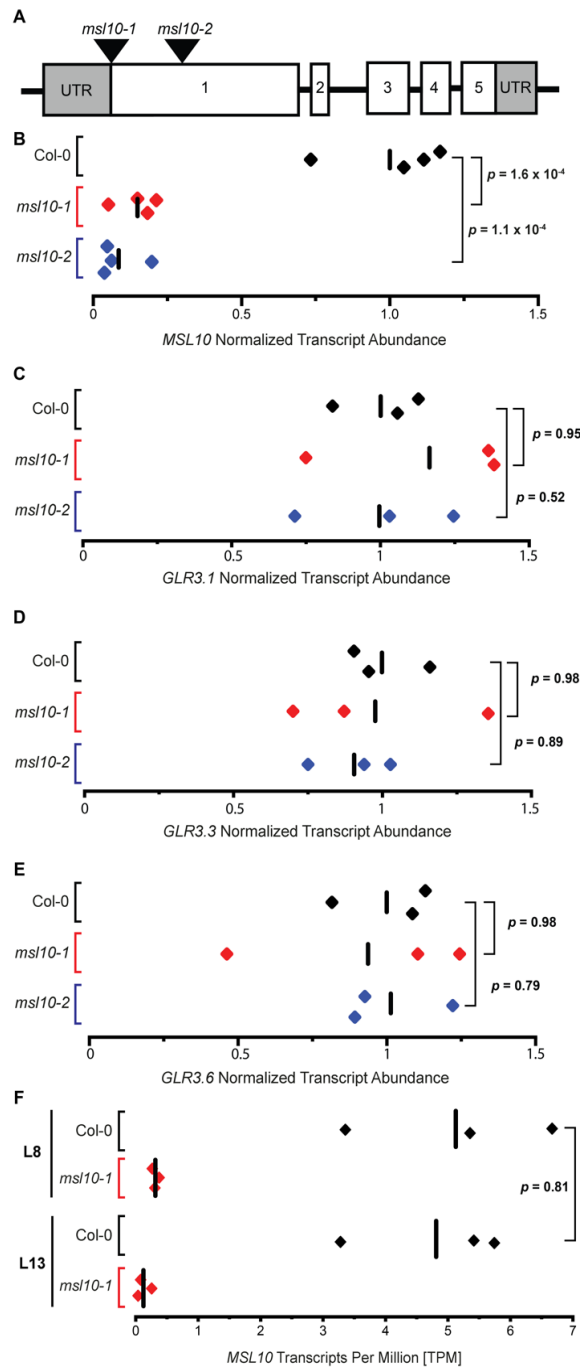
Figure S4. Description and validation of *msl10-1* and *msl10-2* mutant alleles and expression of GLR3s in *msl10-1*. (**A**) Diagram of the *MSL10* genomic locus showing T-DNA insert locations. Untranslated regions (UTR) are shown in grey; exons are numbered. Arrowheads indicate relative T-DNA insertion positions. (**B**) Quantification of residual transcript levels of *MSL10* in the *msl10-1* and *msl10-2* mutant backgrounds by qPCR. Lines show averages; *p*-values generated by Student's t-test, n = 4. (**C-E**) Quantification of baseline transcript levels of genes previously identified as important for SWP generation in Leaf 13. Plotted data show *GLR3.1* (**C**), *GLR3.3* (**D**), and *GLR3.6*. (**E**) Transcript abundance in Col-0, *msl10-1*, and *msl10-2* mutant backgrounds quantified by qPCR. Lines show averages; *p*-values generated by Student's t-test, n = 3. (**F**) Quantification of *MSL10* transcript abundance in Leaf 8 (L8) and Leaf 13 (L13) of Col-0 plants compared to *msl10-1* mutant by RNA-seq. Displayed *p*-value calculated by Student's t-test (n = 3).
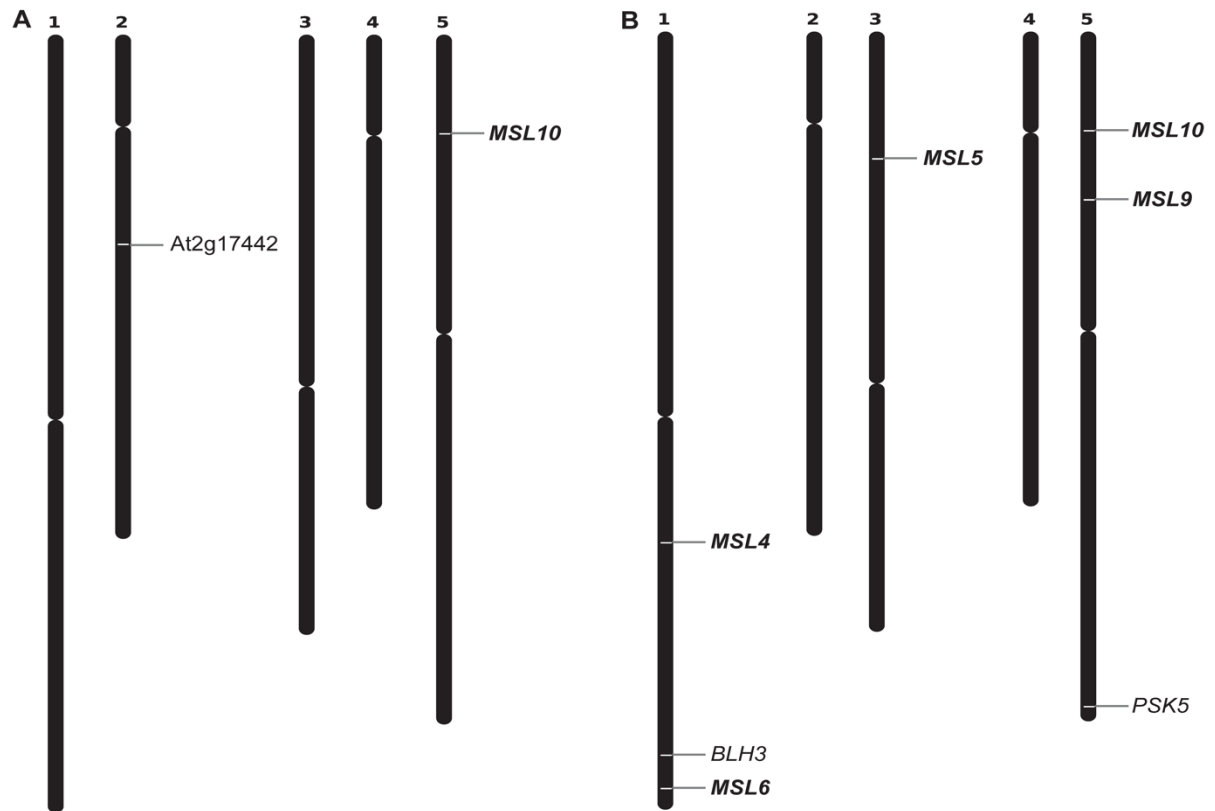
Figure S5. Schematic chromosomal representation and annotation of T-DNA insertion sites in *msl10-1* single and quintuple mutants. **(A)** In addition to the T-DNA insertion in *MSL10*, the single mutant *msl10-1* carries a second insertion in gene At2g17442, coding for a protein of unknown function. (**B**) The *msl* quintuple mutant carries T-DNA insertions in *MSL4*, *5*, *6*, *9,* and *10* and also in genes coding for *BEL1-LIKE HOMEODOMAIN 3 (BLH3)* and for the *PHYTOSULFOKINE SIGNALING PRECURSOR 5* (*PSK5*). For detailed information, refer to Tables S5 and S6.
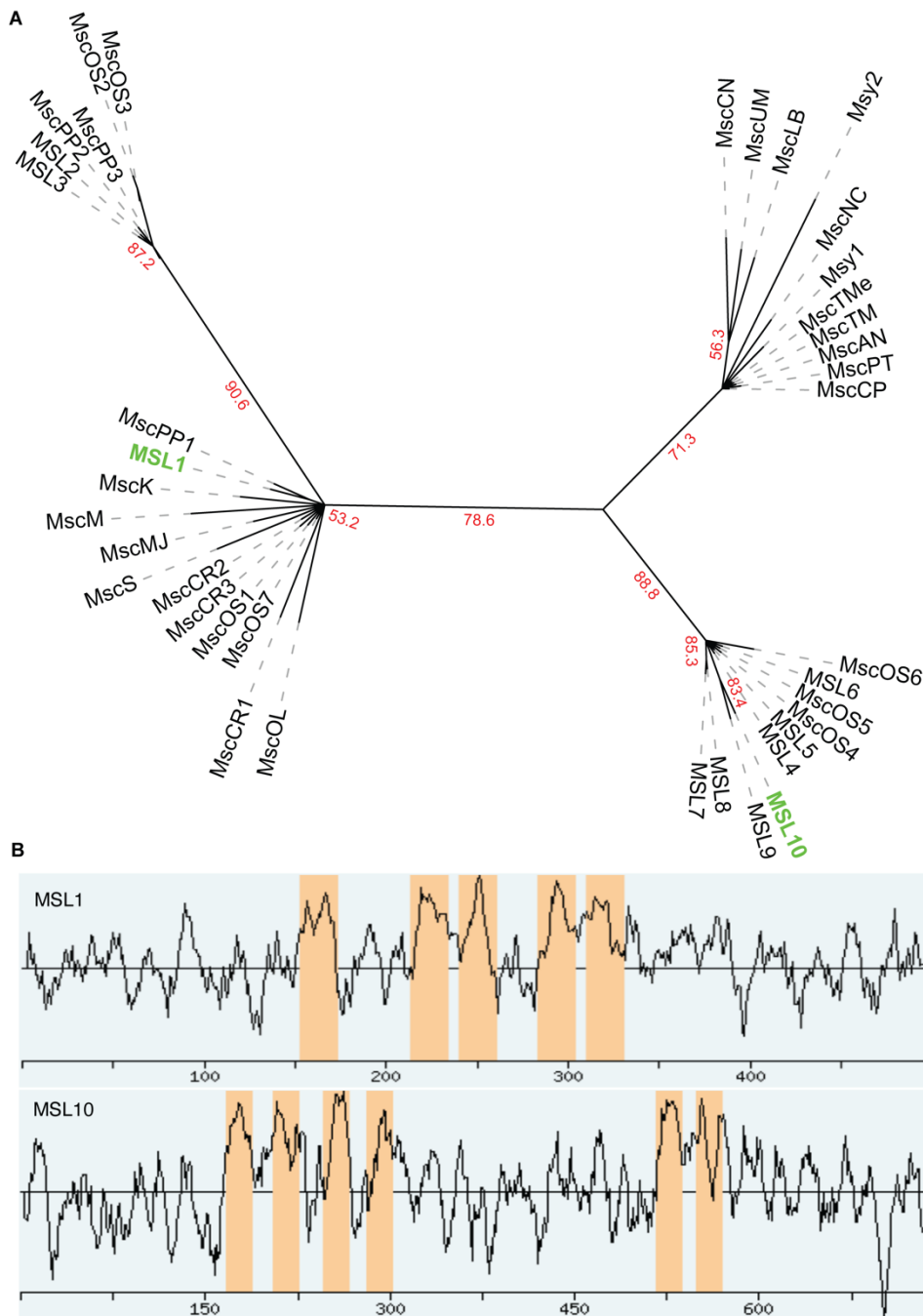
Figure S6. Phylogenetic relationship and hydropathy profiles of selected MscS-like channels. (**A**) The phylogeny of 39 members of the MscS family is presented as an unrooted tree and was generated using the NGPhylogeny tool (https://ngphylogeny.fr) (*53*) and visualized with the help of iTOL (https://itol.embl.de) (*54*), highlighting MSL1 and 10 (green). The full-length protein sequences were aligned using the MAFFT alignment program (*55*) with a gap-opening penalty of 1.53 and a gap-extension penalty of 0.123. The phylogenetic tree was generated using the neighbor-joining method with the LG amino acid replacement matrix. Clade support scores were calculated by bootstrapping (n = 1,000 replicates, red values presented as percentages), and branches with bootstrap values (red) of less than 50% were collapsed. (**B**) Hydropathy profiles (as predicted by AramTmCon (MSL1) and AramTmMultiCon (MSL10), http://aramemnon.uni-koeln.de/) illustrate the number of predicted transmembrane spans (orange bars) in the amino acid sequence of MSL1 (At4g00290, 5 spans, upper panel) and MSL10 (At5g12080, 6 spans, lower panel), respectively.
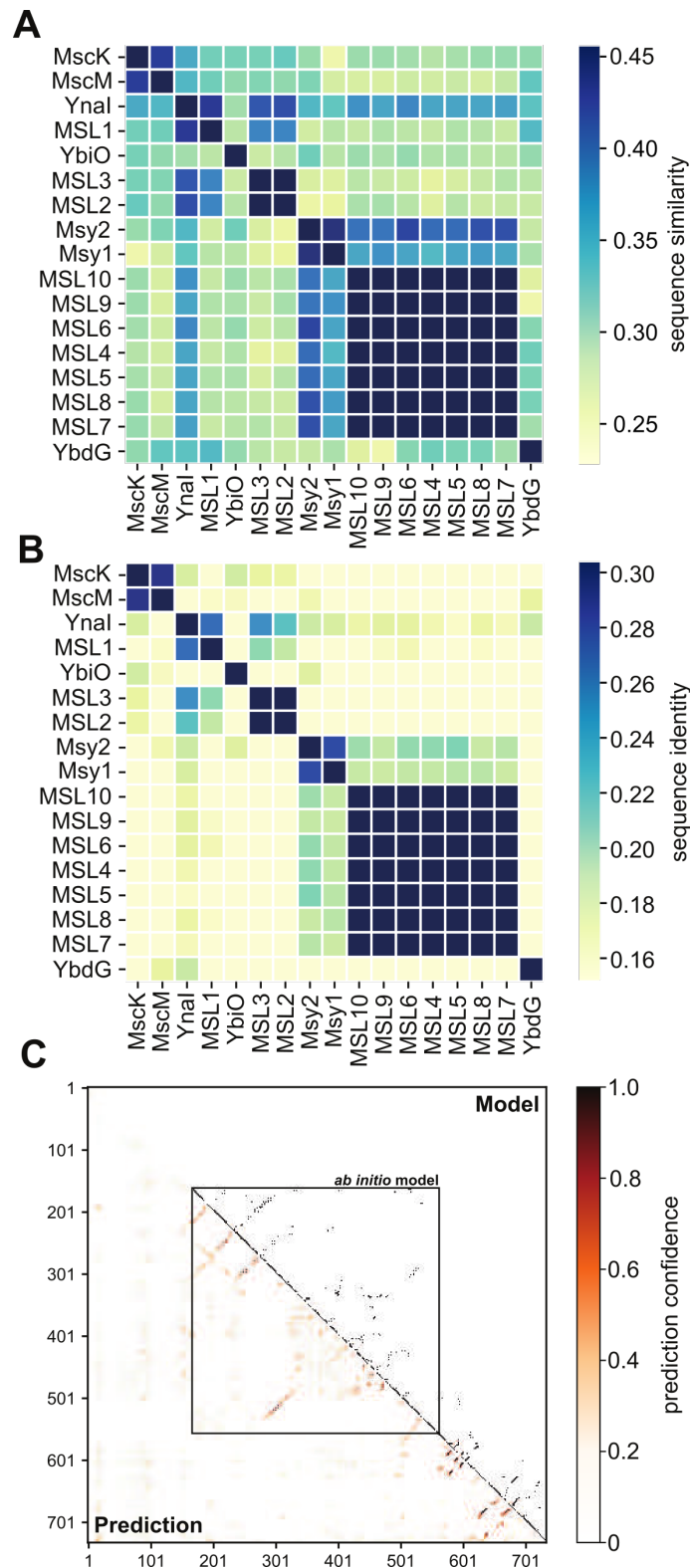
Figure S7. Sequence similarity and identity between selected mechanosensitive channel proteins. (**A**) Pairwise sequence similarities and (**B**) identities between *E. coli* MscK, MscM, YnaI, YbiO, and YbdG, *A. thaliana* MSL1-10, and *S. pombe* Msy1 and Msy2. (**C**) RaptorX[4]-predicted protein contacts (lower left) and contacts obtained from the generated model (upper right). Predicted contacts within the square were used to model the TM part lacking homologous templates.
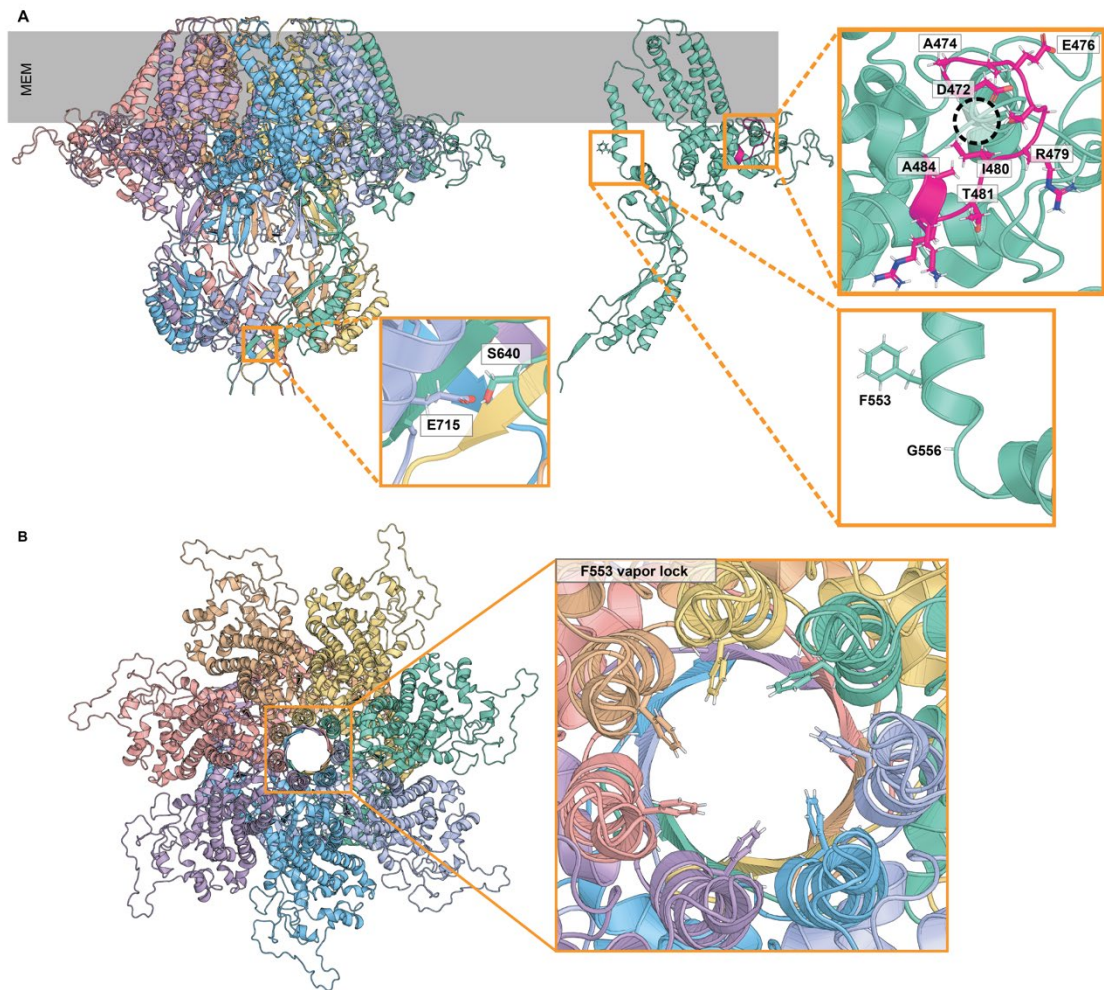
Figure S8. (**A**) Heptameric assembly (left) and monomer (right); membrane embedded as predicted by memembed (*67*). The model shows an extended transmembrane region compared to resolved homologs (*29*, *30*). Key residue S640 forms a hydrogen bond with E715 of the neighboring chain. F553 in TM6 forms the vapor lock of the channel (see also panel B), and the helix kinks at G556; both residues are essential for the function of the channel (*23*). The region with homology to calcyphosin (magenta in **A**) was identified as an EF-hand-derived motif (Fig. S6) and a putative calcium binding site (dashed circle) by IonCom (*63*). (**B**) Top view of the heptameric assembly and a blow-up of the vapor lock, with F553 pointing towards the pore as in MSL1 (*29*).
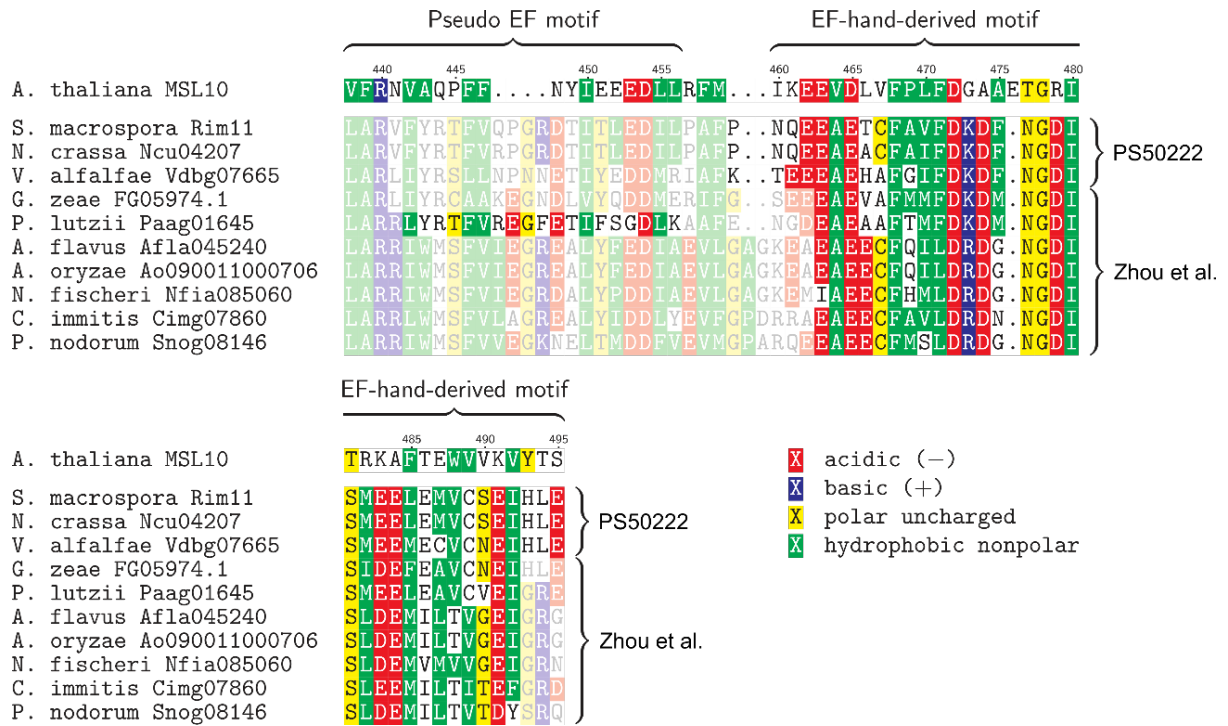
Figure S9. Multiple sequence alignment of the Pseudo EF motif and an EF-hand-derived motif in MSL10 with EF-hand motifs from selected MscS-like proteins containing an EF-hand. Transparent regions show sequence segments in which no EF-hand was identified. Non-transparent regions correspond to either the Pseudo EF motif and the EF-hand-derived motif in MSL10, or a canonical or non-canonical EF-hand in EF-MscS, identified according to PROSITE entry PS50222 or the definitions in (*61*).
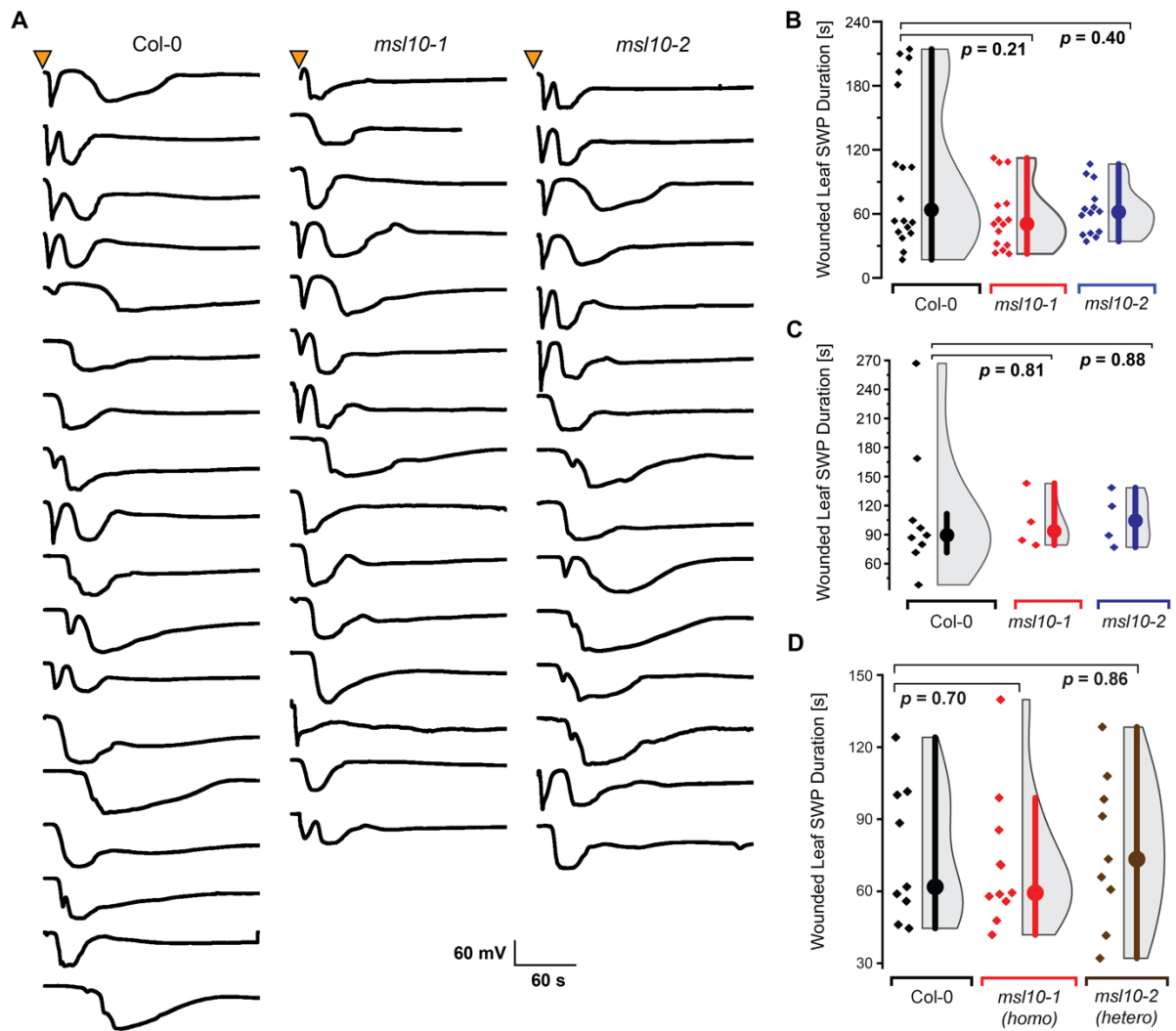
Figure S10. Leaf 8 shows variable wounding responses in both Col-0 and *msl10* mutants. (**A**) Plotted L8 SWP responses after wounding from a single experimental dataset showing Col-0, *msl10-1*, and *msl10-2*. Note the variability between L8 responses just within individual genotypes. Orange arrowhead indicated mechanical wounding of L8. (**B**) SWP duration in L8 after wounding (median ± S.E.M.: Col-0: 97.9 ± 16.7 s, *msl10-1*: 57.0 ± 8.0 s, *msl10-2*: 63.1 ± 6.1 s). Quantification of time course analysis displayed in A and in Fig3A. (**C**) Independent study of SWP duration in L8 after wounding (median ± S.E.M.: Col-0: 97.9 ± 16.7 s, *msl10-1*: 57.0 ± 8.0 s, *msl10-2*: 63.1 ± 6.1 s); *p*-values generated via Student's t-test. (**D**) Third independent study SWP duration in L8 after wounding (median ± S.E.M.: Col-0: 62.0 ± 9.5 s, *msl10-1*: 59.4 ± 8.4 s, *msl10-2*: 73.4 ± 10.5 s). Homozygous (homo) and heterozygous (hetero) mutants were analyzed. Half-violin plots show kernel density estimates (KDEs) calculated using Scott's estimated bandwidth; circle: median; whiskers: 1.5 x IQR Displayed *p*-values generated via Mann-Whitney U test.
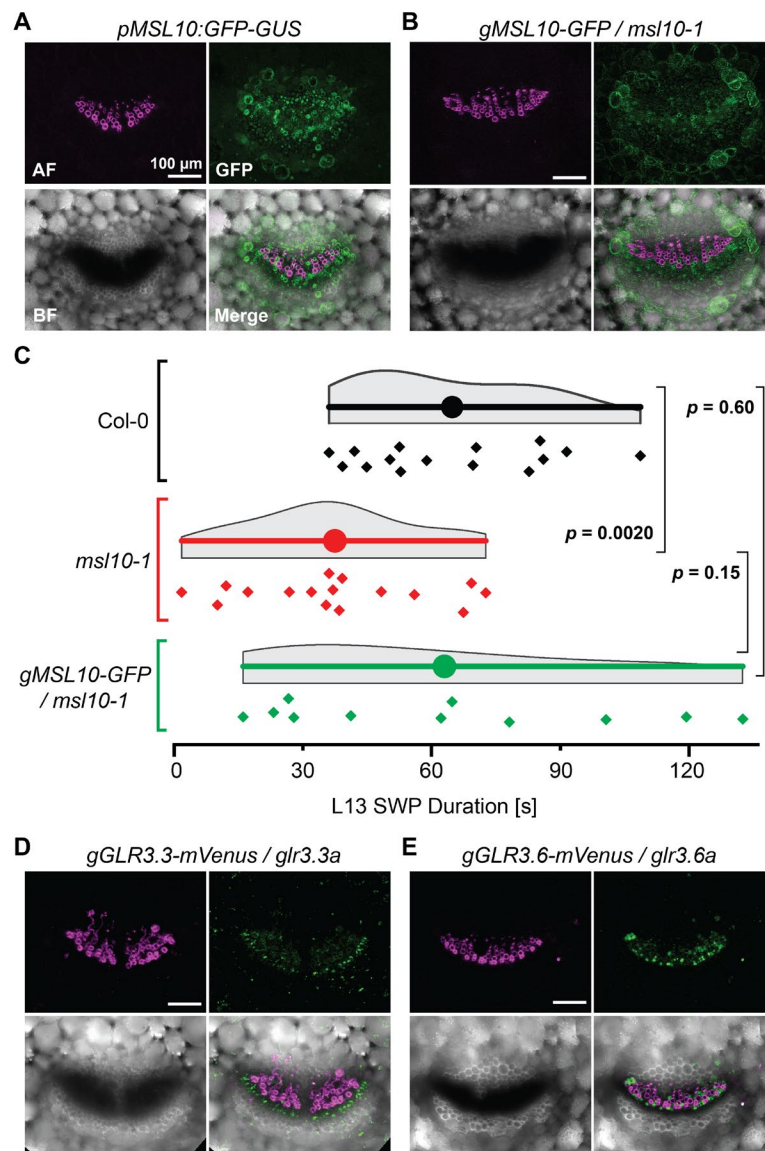
Figure S11. Additional localization data and controls of known SWP-involved components. (**A**) 300 μm petiole sections (maximum intensity z-stack projections) showing GFP localization patterns conferred by a *MSL10* promoter fragment. Lignin autofluorescence (AF; in magenta) and brightfield (BF) images are used as landmarks in order to orient GFP (green) localizations in merged images. (**B**). A petiole section showing localization of GFP-fused to a fully encoding genomic *MSL10* fragment under its native promoter in the *msl10-1* mutant background. Note the consistent anatomical distributions of the expression pattern and protein localization of *MSL10*. (**C**) Quantified SWP durations (median ± S.E.M.: Col-0: 66.7 ± 7.7 s, *msl10-1*: 40.8 ± 3.0 s, *msl10-2*: 72.0 ± 10.0 s). Half-violin plots show kernel density estimates (KDEs) calculated using Scott's estimated bandwidth; circle: median; whiskers: 1.5 x IQR; *p*-values generated via Mann-Whitney U test. (**D**) Transverse sections of *glr3.3a* mutant expressing a genomic *GLR3.3* fragment fused to mVenus under the native *GLR3*.3 promoter. (**E**) Transverse sections of *glr3.6a* mutant expressing a genomic *GLR3.6* fragment fused to mVenus under the native *GLR3.6* promoter. Note the difference in anatomical localization of *GLR3s* in (**D,E**) compared to *MSl10* (**A,B**). Scale bars: 100 μm.
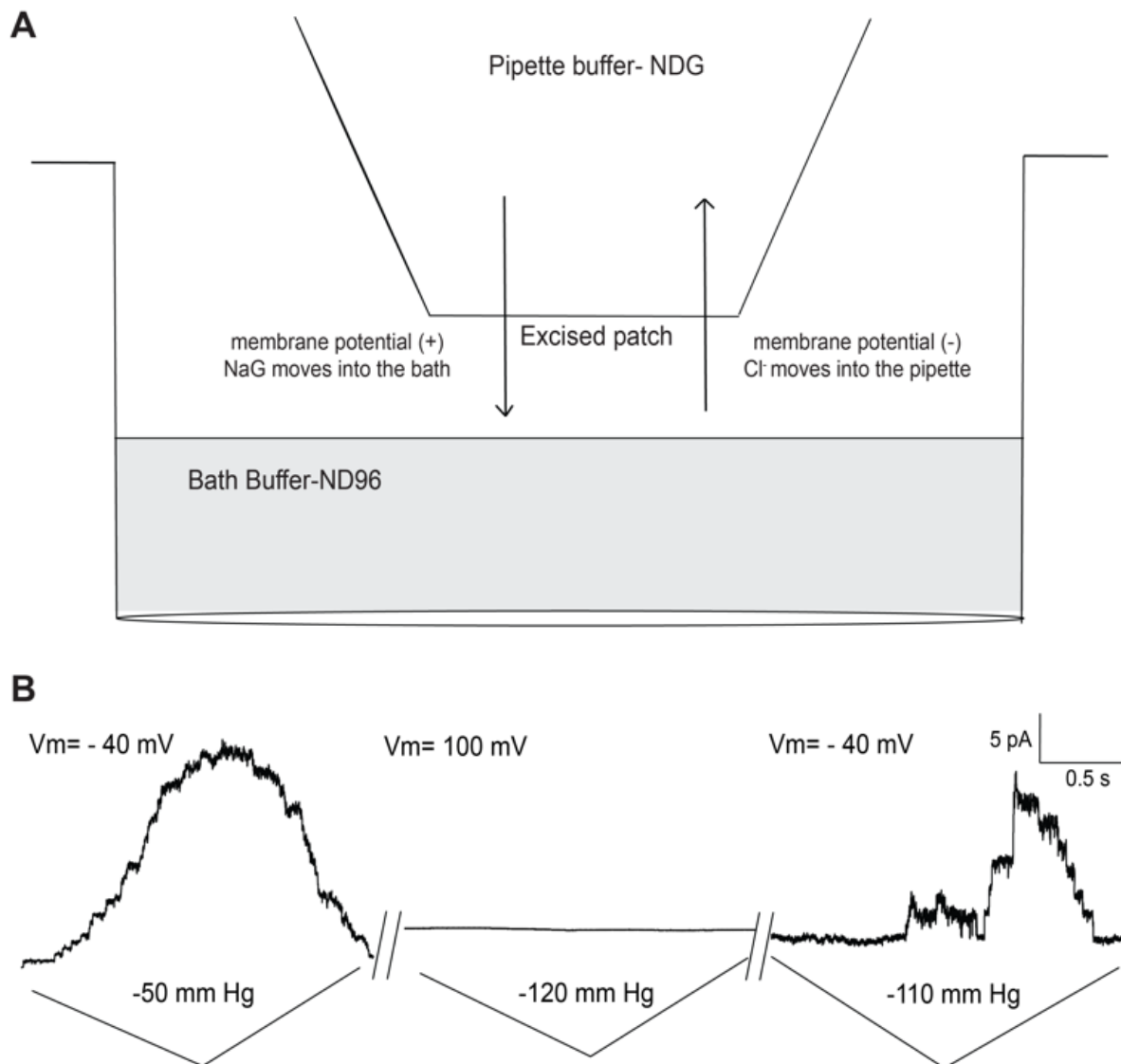
Figure S12. MSL10 does not conduct glutamate in excised patches from *Xenopus* oocytes. (A) Schematic representation depicting the setup used for testing glutamate conductivity. Under negative membrane voltage, chloride ions can move into the pipette from the bath through MSL10. Positive membrane voltage would drive glutamate anions into the bath from the pipette if MSL10 were to conduct glutamate. Bath, ND96; pipette solution, NDG (similar to ND96 but NaCl and KCl replaced by sodium glutamate). Channels were gated by negative tension (indicated in mmHg) by applying repeated, symmetric 5-s pressure ramps (indicated as a triangle). **(B)** Traces of MSL10 channel activity in an inside-out, excised patch at a negative membrane potential (left trace, - 40 mV) in asymmetric buffer condition. No tension-induced MSL10-dependent current was recorded when the patch was clamped at positive membrane potential (middle trace, 100 mV). Upon reverting back to negative membrane potential, MSL10-dependent currents were again recorded (right trace, - 40 mV).
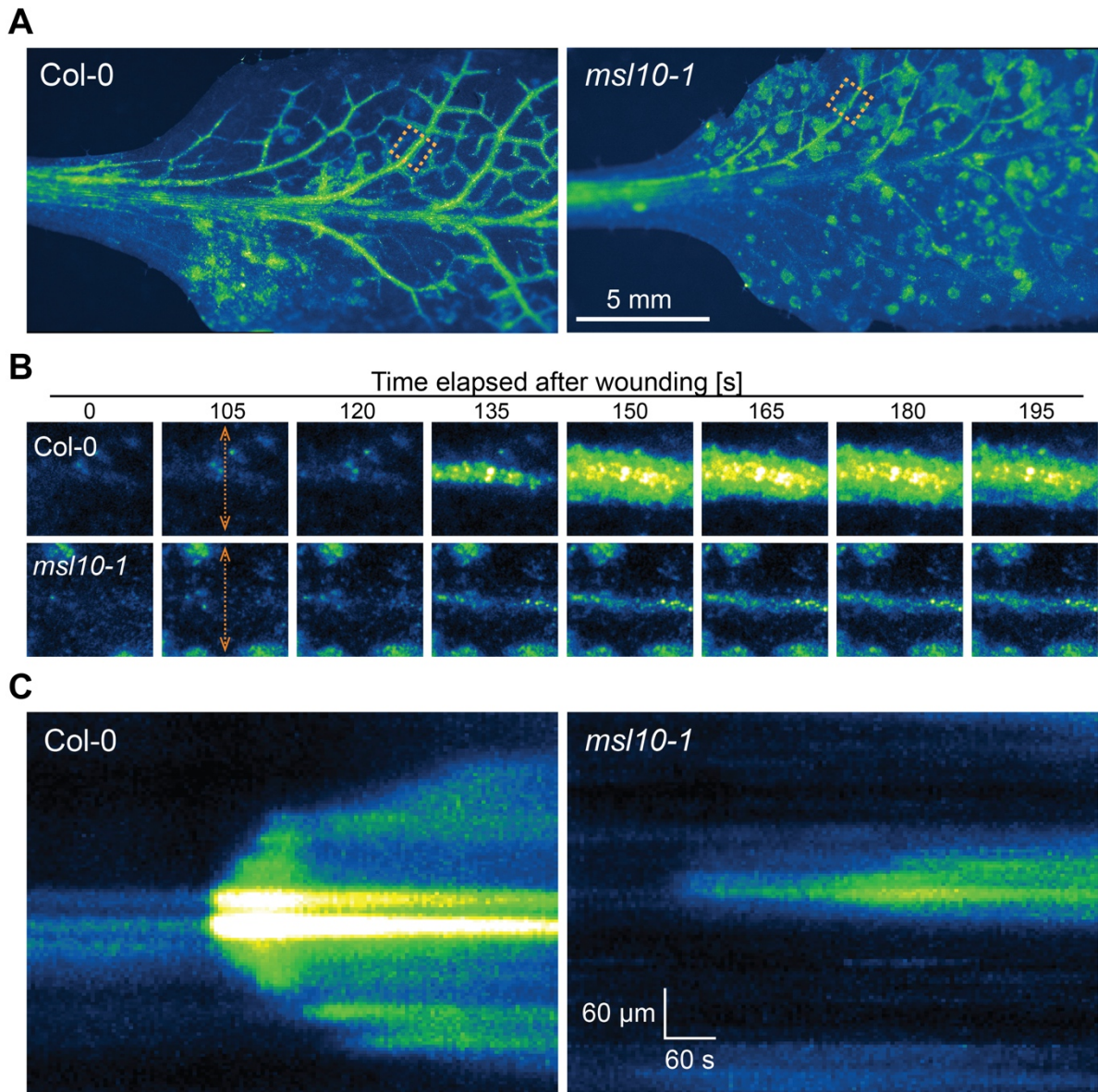
Figure S13. The spread of wound-induced cytosolic calcium elevations from MatryoshCaMP6s-expressing Arabidopsis leaf 13 veins is impaired in *msl10-1* mutants. (A) Representative images of *msl10-1* mutants show lower levels of maximum MatryoshCaMP6s fluorescence in L13 veins after wounding relative to Col-0. (**B**) Close-up of the region of interest (ROI, dotted orange rectangle) from (A) of a secondary vein showing reduced levels of fluorescence increase in *msl10-1* mutants after wounding. (**C**) Kymograph of the ROI transect drawn in (B) showing how the initial change in fluorescence occurs in the veins and proceeds to flare outwardly in Col-0, whereas the flare is attenuated in *msl10-1* mutants.
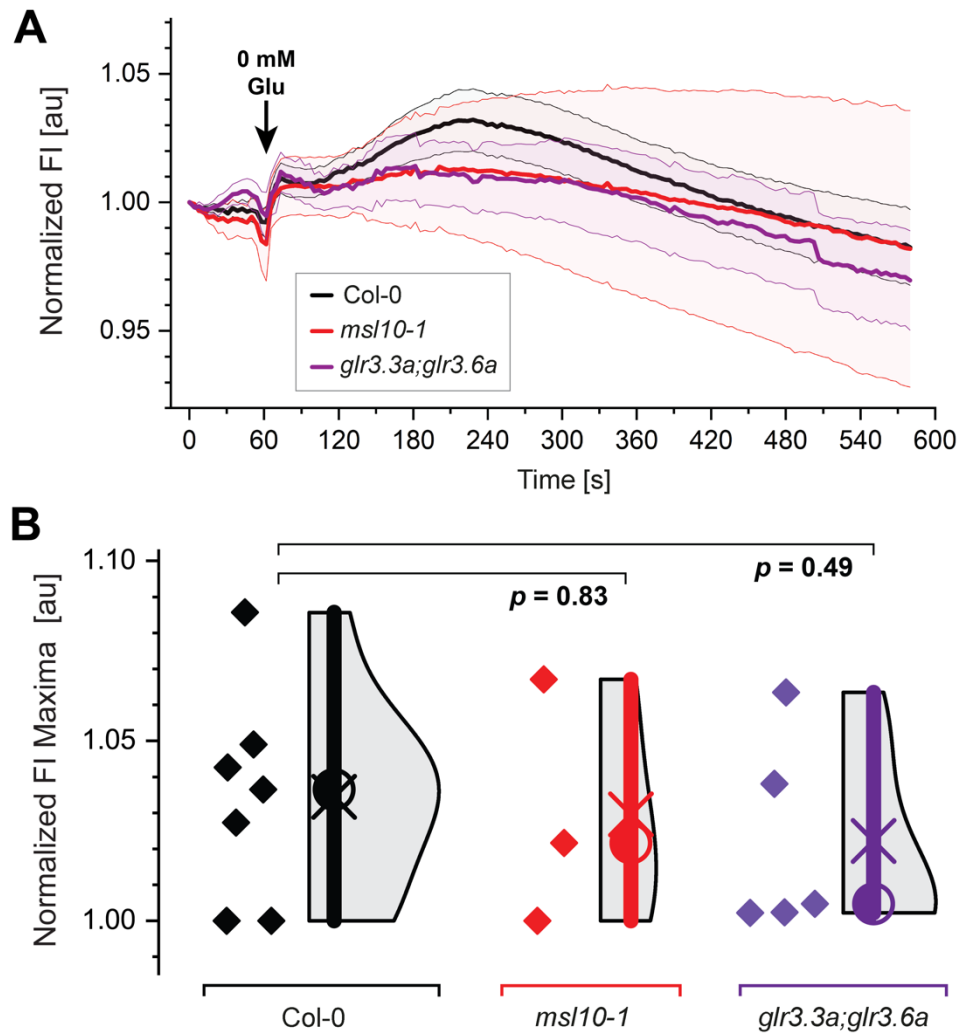
Figure S14. Results of mock treatments of leaves as control for glutamate treatment experiments. (**A**) Time course analysis showing mean and SEM per genotype. (**B**) Quantification and statistical analysis of maximal response to mock treatment. Mock treatments were a negative control for data presented in Fig. 10 and were imaged under identical conditions. Displayed *p*-values calculated by Student's t-test (n = 3 - 7).
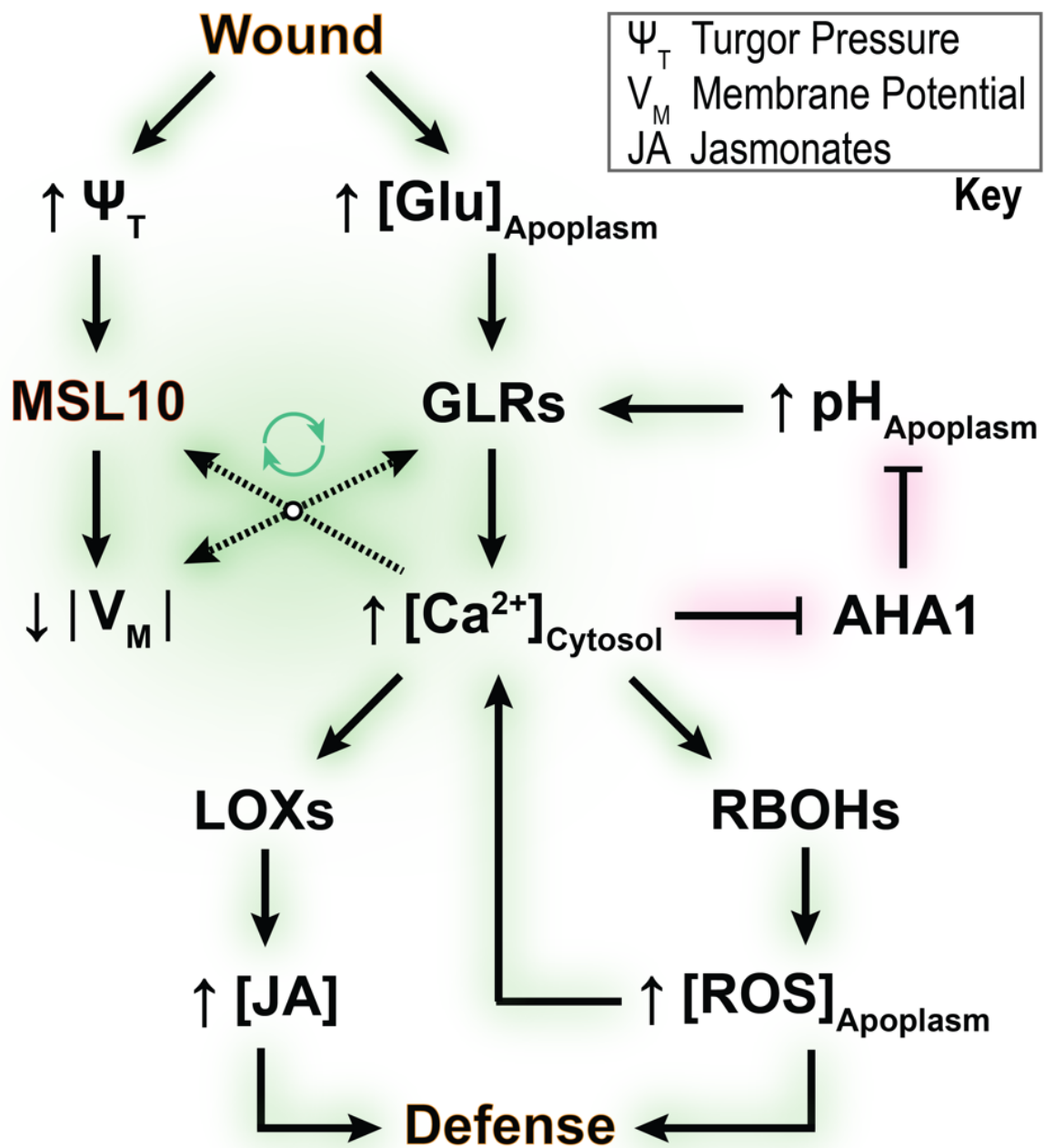
Figure S15. Hypothetical mechanistic model for role of MSL10 in wound signaling. Wounding triggers concomitant glutamate (Glu) release and an internal pressure (ψ_T) wave. Membrane stretching activates MSL10-mediated anion efflux, depolarizing the membrane potential ($|V_M|$). GLRs are activated by concomitant Glu accumulation in the apoplasm and membrane depolarization. GLR-mediated Ca^{2+} influx inactivates the H^+-ATPase AHA1, causing sustained membrane depolarization and apoplasmic alkalinization, which stimulates GLR channel activity and may prolong MSL10 activation via an EF-hand-like motif identified in this study (feedback loop for mutual potentiation, green arrows). Ca^{2+} triggers respiratory burst oxidase homologs (RBOHs), JA-synthesizing lipoxygenases (LOXs) and a rise in reactive oxygen species (ROS), contributing to plant defense.

Table S1. Arabidopsis lines screened for defects in wound-induced SWP. Description of genotype, genomic locus accession number, predicted or known function/activity, stock identification number, and seed source are provided for each line.

Genotype	Mutated Gene(s)	Function/Activity	Stock ID	Source
akt2	AT4G22200	Plasma membrane voltage-gated K$^+$-channel	SALK_103567	SALK
ald1	AT2G13810	L-lysine α-amino transferase	SALK_007673	SALK
ann1	AT1G35720	Annexin Ca^{2+}/phospholipid-binding protein	SALK_015426	SALK
ann2	AT5G65020	Annexin Ca^{2+}/phospholipid-binding protein	SALK_054223	SALK
ann3	AT2G38760	Annexin Ca^{2+}/phospholipid-binding protein	SALK_082344	SALK
ann4	AT2G38750	Annexin Ca^{2+}/phospholipid-binding protein	SALK_019725	SALK
ann8	AT5G12380	Annexin Ca^{2+}/phospholipid-binding protein	SALK_062276	SALK
cngc12	AT2G46450	Cyclic nucleotide-gated cation channel	SALK_092622	SALK
dorn1	AT5G60300	Plasma membrane ATP receptor kinase	*dorn1-2*	*(73)*
gad1;gad2	AT5G17330; AT1G65960	Glutamate decarboxylase	SALK_017810, GK_474E05	*(74)*
glr3.1	AT2G17260	Glutamate receptor-like ion channel	SALK_063873	*(3)*
glr3.3	AT1G42540	Glutamate receptor-like ion channel	SALK_077608	*(3)*
glr3.6	AT3G51480	Glutamate receptor-like ion channel	SALK_091801	*(3)*
glr3.3;glr3.6	AT1G42540 AT3G51480	Glutamate receptor-like ion channels	SALK_077608 SALK_091801	*(3)*
msl4;msl5;msl6	AT1G53470 AT3G14810 AT1G78610	Plasma membrane mechanosensitive ion channels	SALK_142497 SALK_127784 SALK_067711	*(18)*
msl10-1	AT5G12080	Plasma membrane mechanosensitive ion channel	SALK_076254	*(18)*
msl10-2	AT5G12080	Plasma membrane mechanosensitive ion channel	SAIL_292_B11	SALK
mslΔ5	AT1G53470 AT3G14810 AT1G78610 AT5G12080 AT5G19520	Plasma membrane mechanosensitive ion channels	SALK_142497 SALK_127784 SALK_067711 SALK_114626 SALK_076254	*(18)*
pepr1;pepr2	AT1G73080 AT1G17750	Plasma membrane peptide receptor kinases	SALK_059281 SALK_098161	*(75)*
pop2	AT3G22200	γ-amino-butyrate (GABA) transaminase	GK_157D10	*(74)*
rbohb;rbohf	AT1G09090 AT4G03560	Plasma membrane NADPH oxidases	-	N. Geldner
slah3-3	AT5G24030	Plasma membrane anion channel	SALK_106054	*(76)*
tmem16	AT1G73020	Ion channel and/or phospholipid scramblase	SALK_012541	SALK
tpc1	AT4G03560	Two-pore slow vacuolar cation channel	SALK_145413	*(72)*
Ws ecotype	-	-	-	S. Roux
Col-0 ecotype	-	-	CS70000	SALK

Table S2. Number of SWP recordings, sample sizes, and number of cases in which an expected genotype-specific SWP was observed in blinded experiments. Starting dates for each batch of experiments are provided in yy.mm.dd format. Location (Loc.) abbreviations are Stanford (S), Düsseldorf (D), and Lausanne (L). The number of events wherein no depolarization was detected (N), a wild-type-like SWP was recorded (W), or a shortened-duration depolarization was detected (S, typically <50 s) are provided, along with the total sample size (n).

Date	Loc.	Col-0	msl10-1	msl10-2	mslΔ5	msl4;5;6	glr3.3	glr3.6
		N / W / S / n	N / W / S / n	N / W / S / n	N / W / S / n	N / W / S / n	N / W / S / n	N / W / S / n
18.01.03	S	1 / 14 / 4 / 19			0 / 3 / 16 / 19			
18.04.23	S	0 / 16 / 0 / 16			0 / 0 / 7 / 7			
18.04.27	S	0 / 7 / 1 / 8	0 / 0 / 8 / 8					
18.12.12	D	0 / 3 / 1 / 4	0 / 1 / 3 / 4					
19.01.19	S	0 / 8 / 2 / 10	2 / 1 / 6 / 9	0 / 2 / 7 / 9				
19.01.27	S	0 / 6 / 2 / 8	0 / 0 / 6 / 6					
19.02.10	S	0 / 10 / 3 / 13	0 / 0 / 13 / 13	0 / 0 / 12 / 12				
19.03.03	S	1 / 6 / 1 / 8	0 / 0 / 10 / 10					
19.04.23	S	0 / 6 / 3 / 9	0 / 2 / 5 / 7			0 / 6 / 3 / 9		
19.06.12	S	5 / 22 / 6 / 33	0 / 2 / 20 / 22					
19.06.25	S	0 / 11 / 6 /17	3 / 1 / 12 / 16				2 / 3 / 6 / 11	0 / 1 / 13/ 14
19.11.16	S	7 / 6 / 1 / 14	5 / 2 / 7 / 14	3 / 3 / 10 / 16				
20.01.23	S	1 / 6 / 3 / 10	3 / 0 / 7 / 10	4 / 2 / 4 / 10			1 / 0 / 6 / 7	
20.01.25	S	2 / 5 / 0 / 7	1 / 0 / 6 / 7					
20.02.25	L	3 / 14 / 3 / 20	1 / 1 / 14 / 16	7 / 1 / 7 /15				
20.02.29	D	2 / 10 / 0 / 12	0 / 0 / 4 / 4	0 / 0 / 4 / 4				

Table S3. Summary of the statistics for SWP data presented in figures. Parameters are described in the main text and main text figure legends and defined in materials and methods. IQR stands for interquartile region. Standard error of mean (S.E.M.) values and *p*-values were calculated using Origin Pro 2020.

mslΔ5 L13	Duration (s)		Derivative (mV / s)		Amplitude (mV)		Hyperpolarization (mV)	
	Col-0	*mslΔ5*	Col-0	*mslΔ5*	Col-0	*mslΔ5*	Col-0	*mslΔ5*
Mean	79.1	20.8	-26.5	-19.0	-46.8	-55.2	15.2	6.7
S.E.M.	12.1	1.7	2.5	1.9	4.0	6.4	3.5	2.3
Median	82.6	20.3	-27.7	-18.2	-43.9	-50.3	11.6	5.1
1.5 * IQR	86.4	8.1	14.7	4.2	22.5	33.6	15.0	13.2
Mann-Whitney U-test *p*		2.1×10^{-02}		8.9×10^{-02}		3.7×10^{-01}		1.0×10^{-01}
Student's t-test *p*		5.0×10^{-03}		8.2×10^{-02}		2.6×10^{-01}		1.4×10^{-01}
Sample Size (*n*)	16	7	16	7	16	7	16	7

msl10 L13	Duration (s)			Amplitude (mV)			Derivative (mV / s)		
	Col-0	*msl10-1*	*msl10-2*	Col-0	*msl10-1*	*msl10-2*	Col-0	*msl10-1*	*msl10-2*
Mean	92.2	28.8	32.8	-48.2	-48.9	-44.0	-42.5	-45.1	-37.9
S.E.M.	11.8	7.0	5.9	3.2	4.7	4.0	3.9	4.6	4.9
Median	99.6	21.7	32.7	-46.4	-59.4	-43.7	-43.8	-52.3	-38.3
1.5 * IQR	88.5	31.9	38.4	35.7	28.2	14.8	33.3	38.3	34.0
Mann-Whitney U-test *p*		3.6×10^{-03}	1.8×10^{-02}		6.5×10^{-01}	1.9×10^{-01}		2.0×10^{-01}	5.0×10^{-01}
Student's t-test *p*		8.8×10^{-05}	4.5×10^{-03}		4.7×10^{-01}	6.0×10^{-01}		2.8×10^{-01}	4.3×10^{-01}
Sample Size (*n*)	20	17	8	17	15	8	17	14	8
	Hyperpolarization (mV)			Repolarization Max. (mV)			Velocity (cm / min)		
	Col-0	*msl10-1*	*msl10-2*	Col-0	*msl10-1*	*msl10-2*	Col-0	*msl10-1*	*msl10-2*
Mean	17.2	21.4	18.8	-3.3	12.1	5.5	10.9	11.3	11.6
S.E.M.	2.1	2.1	2.1	1.5	3.6	2.7	1.0	0.8	0.8
Median	17.1	20.6	20.6	-4.0	12.5	4.0	10.7	10.9	12.1
1.5 * IQR	14.9	8.8	15.0	7.5	25.5	6.4	7.8	7.4	5.5
Mann-Whitney U-test *p*		1.0×10^{-01}	4.0×10^{-01}		4.2×10^{-04}	4.4×10^{-03}		9.2×10^{-01}	7.9×10^{-01}
Student's t-test *p*		1.2×10^{-01}	6.4×10^{-01}		1.3×10^{-04}	1.9×10^{-03}		8.9×10^{-01}	6.7×10^{-01}
Sample Size (*n*)	17	15	8	17	15	8	17	15	8

msl10 L8	L8 Duration (s)		
	Col-0	*msl10-1*	*msl10-2*
Mean	97.9	57.0	63.1
S.E.M.	16.7	8.0	6.2
Median	63.8	50.6	61.6
1.5 * IQR	177.1	56.0	44.7
Mann-Whitney U-test *p*		2.1×10^{-01}	4.0×10^{-01}
Student's t-test *p*		4.6×10^{-02}	8.8×10^{-02}
Sample Size (*n*)	18	15	14

msl10-1;glr3 L13	L13 Duration (s)			
	Col-0	*msl10-1*	*msl10-1;glr3.3*	*msl10-1;glr3.6*
Mean	95.0	36.1	35.7	24.3
S.E.M.	10.5	6.1	5.1	4.5
Median	83.7	30.1	33.8	22.8
1.5 * IQR	73.4	60.1	19.7	36.7
Mann-Whitney U-test *p*		1.8×10^{-04}	2.2×10^{-04}	1.0×10^{-06}
Student's t-test *p*		1.7×10^{-04}	1.2×10^{-04}	1.1×10^{-05}
Sample Size (*n*)	17	12	12	12

Table S4. Genomic characterization of *msl10-1* T-DNA insertion mutant. In addition to the T-DNA insertion in exon 1 of *MSL10* (At5g12080), the single mutant carries a second insertion in the promoter region/ 5'-UTR of gene At2g17442, which encodes a protein of unknown function.

Insertion	Insertion Site	Chromosome	Insert Start Site (bp)	Annotation	Inserted Into	# Support Reads
1	At2g17442	1	7575790	hypothetical protein of unknown function	5'-UTR/promoter	28
2	At5g12080	2	3900881	MSL10	exon 1	32

Table S5. Genomic characterization of *mslΔ5* T-DNA insertion mutant. In addition to T-DNA insertions in the respective first exons of *MSL4*, *5*, *6*, *9* and *10,* the *msl* quintuple mutant also carries T-DNA insertions in the promoter region of a gene coding for *BEL1-LIKE HOMEODOMAIN 3* (*BLH3*) and in the 3'-UTR of the *PHYTOSULFOKINE SIGNALING PRECURSOR 5* (*PSK5*).

Insertion	Insertion Site	Chromosome	Insert Start Site (bp)	Annotation	Inserted into	# Support Reads
1	At1g53470	1	19958655	MSL4	exon 1	13
2	At1g75410	1	28303108	BEL1-LIKE HOMEO-DOMAIN 3 (BLH3)	promoter	32
3	At1g78610	1	29571351	MSL6	exon 1	17
4	At3g14810	3	4973727	MSL5	exon 1	26
5	At5g12080	5	3900881	MSL10	exon 1	39
6	At5g19520	5	6586620	MSL9	exon 1	13
7	At5g65870*	5	26352525	PHYTOSULFOKINE SIGNALING PRE-CURSOR 5 (PSK5)	3'-UTR	15

* A T-DNA was also found to be inserted into the promoter region of At5g65880 (coding for a protein of unknown function) in *mslΔ5*, thereby possibly affecting its gene product.

Table S6. Oligonucleotide primer sequences used in this study. Gene names correspond to names and accessions provided in Table S1.

Gene	Mutant ID	Primer Name	Sequence (5' – 3')
akt2	SALK_103567	LP	TGATAGAAGTCGAAAGCAGCGD
		RP	AGCATCGAGGAAAAGGAAGAG
ald1	SALK_007673	LP	TTACGATGCATTTGCTATGACC
		RP	TTTTAAATGGAACGCAAGGAG
ann1	SALK_015426	LP	TGTTGTTGGTCTCCCTTTTTG
		RP	AATCTTGGCTCACAGAAGTGC
ann2	SALK_054223	LP	TGGGATCAATCTTTTGGTCTG
		RP	GATGCTTGCAAGATCTGAAGC
ann3	SALK_082344	LP	TCCTCAAAACGAAAAATCTCG
		RP	CATAGCCGCCTCAATAGTAGC
ann4	SALK_019725	LP	CTCGGTGCACGTAAAGCTTAC
		RP	AGGTGAAATTCGGTTGGAATC
ann8	SALK_062276	LP	AGGATGATCTGGGTCCTCTTG
		RP	CAAAATTGCCAGAGAGCTCAG
cngc12	SALK_092622	LP	ATTGATGCATTGAAGTCAGGG
		RP	TACTTTGGTTTCGAAGCTTGC
dorn1	*dorn1-2*	seqFor	CATGAGATGTCTGAAACACAGGAATC
		seqRev	AGTTCTTAGTGTCTATTGTCTGTCCC
gad1	SALK_017810	LP	GTGGACTGACTTACCTCGTGG
		RP	GGAGCCAATGTTCAAGTAACG
gad2	GK_474E05	LP	TATCACGCTAACACCTAACGC
		RP	TTCAAGGTTTGTCGGTATTGG
glr3.1	SALK_063873	LP	AGATGAACAAACGTGACCACC
		RP	TGGCTTTTTGTGGTTCTGATC
glr3.3	SALK_077608	LP	TGCTGTTGATCTCTTGCAATG
		RP	CACACAACCATATGCAGCATC
glr3.6	SALK_091801	LP	TTCGTTCAAAGGTGGCATAAC
		RP	CGACTATGAGGAAAGACGCAG
msl4	SALK_142497	LP	AATTCATTATCACATTCGCGC
		RP	GCGTGACTCTGTTCTGTCTCC
msl5	SALK_127784	LP	CCCTCATCTTCTTCTTTGATCG
		RP	ACTTCCCATTTCCACAAATCC
msl6	SALK_067711	LP	TCCCTTTGTTTTCTCCTCCTC
		RP	CGAAGCTGATTGGTCAGTTTC
msl9	SALK_114626	LP	CGGTGTCAAGCATGTGTTATG
		RP	AGGTCCCGAGAGAGTCTGAAG
msl10-1	SALK_076254	LP	GTTGGTTTCTGGGTTTAAGCC
		RP	TACTTGGAGTAACCGGTGCTG
msl10-2	SAIL_292_B11	LP	GGCTGAGCAACATTTCTGAAG
		RP	AGGAAATCTTTTGCAAGGTCG
pepr1	SALK_059281	LP	TTTCACCTGTCAATCCGTTTC
		RP	TCGTTTCGGATCACCTAATTG
pepr2	SALK_098161	LP	AGCGTCCAAAGAAGCTTTCTC
		RP	TGCCTATCTCAGGTGGAACAC
pop2	GK_157D10)	LP	TTGTCACAGCCAAACATTGTC
		RP	TTTTTACAAGCGGTGGATCAG
rbohb	SAIL_749_B11	LP	TCCAAATTTGGACATTGCATAG
		RP	AGCTTGGACTTGGTCCTTAGC
rbohf	SALK_059888	LP	TCTCTATTGTATCTTGTGTCACCG
		RP	ACTTGGTCCTTAGCCAAGTGATAG
slah3-3	SALK_106054	LP	ATCTCTTCTTGAGGCTGCGAC
		RP	TTTGTTTTCCTTCGCATATGC
tmem16	GABI_238B02	LP	AATCTCGGAAATGAGAGAGCC
		RP	AATCATTCCAAACTGCAAAGC
tpc1	SALK_145413	LP	ATATCGAAGAAAGCTCGGCTC
		RP	GGGAAATAGAACCCGTGAGAG

SALK	Border Primer	BP	ATTTTGCCGATTTCGGAAC
SAIL	Border Primer	LB	TAGCATCTGAATTTCATAACCAATCTCGATACAC
UBC21	-	qPCRFor	CAGTCTGTGTGTAGAGCTATCATAGCAT
	-	qPCRRev	AGAAGATTCCCTGAGTCGCAGTT
JAZ10		qPCRFor	ATCCCGATTTCTCCGGTCCA
		qPCRRev	ACTTTCTCCTTGCGATGGGAAGA

Legends to Supplementary Movies

Supplementary Movie 1: Calcium imaging of 5-week-old plant (Col-0 background) stably expressing the MatryoshCaMP6s calcium sensor. Wounding L8 (bottom) triggers cytosolic calcium elevations that predominantly spread to neighboring parastichous leaves. Fluorescence intensity is displayed using ImageJ Green Fire Blue lookup table (LUT). Time stamp is in mm:ss format. Scale bar: 5 mm.

Supplementary Movie 2: Calcium imaging of 5-week-old plant (*msl10-1* mutant background) stably expressing the MatryoshCaMP6s calcium sensor. Leaf 8 was wounded (bottom). Fluorescence intensity is displayed using ImageJ Green Fire Blue lookup table (LUT) with brightness and contrast adjusted identically to Suppl. Movie 1. Time stamp is in mm:ss format. Scale bar: 5 mm.

Supplementary Movie 3: Close-up of wound-induced calcium elevations in distal L13 after wounding L8. A 5-week-old Col-0 plant stably expressing the MatryoshCaMP6s calcium sensor was used. Fluorescence intensity is displayed using ImageJ Green Fire Blue LUT. Time stamp is in mm:ss format. Scale bar: 5 mm.

Supplementary Movie 4: Close-up of wound-induced calcium elevations in distal L13 after wounding L8. A 5-week-old Col-0 plant stably expressing the MatryoshCaMP6s calcium sensor was used. Fluorescence intensity is displayed using ImageJ Green Fire Blue LUT with brightness and contrast adjusted identically to Suppl. Movie 3. Time stamp is in mm:ss format. Scale bar: 5 mm.

Supplementary Movie 5: Calcium imaging of L8 of a 5-week-old Col-0 plant stably expressing the MatryoshCaMP6s calcium sensor shows initiation of cytosolic calcium elevations at the site of wounding and transmission through the vasculature. Fluorescence intensity is displayed using ImageJ Green Fire Blue LUT. Time stamp is in mm:ss format. Scale bar: 5 mm.

Supplementary Movie 6: Calcium imaging of L8 of a 5-week-old *msl10-1* plant stably expressing the MatryoshCaMP6s calcium sensor shows initiation of cytosolic calcium elevations at the site of wounding and transmission through the vasculature. Fluorescence intensity is displayed using ImageJ Green Fire Blue LUT with brightness and contrast adjusted identically to Suppl. Movie 5. Time stamp is in mm:ss format. Scale bar: 5 mm.

REFERENCES AND NOTES

1. P. Walch-Liu, L.-H. Liu, T. Remans, M. Tester, B. G. Forde, Evidence that l-glutamate can act as an exogenous signal to modulate root growth and branching in *Arabidopsis thaliana*. *Plant Cell Physiol.* **47**, 1045–1057 (2006).

2. M. Toyota, D. Spencer, S. Sawai-Toyota, W. Jiaqi, T. Zhang, A. J. Koo, G. A. Howe, S. Gilroy, Glutamate triggers long-distance, calcium-based plant defense signaling. *Science* **361**, 1112–1115 (2018).

3. S. A. R. Mousavi, A. Chauvin, F. Pascaud, S. Kellenberger, E. E. Farmer, *GLUTAMATE RECEPTOR-LIKE* genes mediate leaf-to-leaf wound signalling. *Nature* **500**, 422–426 (2013).

4. D. E. Featherstone, S. A. Shippy, Regulation of synaptic transmission by ambient extracellular glutamate. *Neuroscientist* **14**, 171–181 (2008).

5. G. Lohaus, K. Pennewiss, B. Sattelmacher, M. Hussmann, K. Hermann Muehling, Is the infiltration-centrifugation technique appropriate for the isolation of apoplastic fluid? A critical evaluation with different plant species. *Physiol. Plant.* **111**, 457–465 (2001).

6. G. Pilot, H. Stransky, D. F. Bushey, R. Pratelli, U. Ludewig, V. P. Wingate, W. B. Frommer, Overexpression of *GLUTAMINE DUMPER1* leads to hypersecretion of glutamine from hydathodes of Arabidopsis leaves. *Plant Cell* **16**, 1827–1840 (2004).

7. M. M. Wudick, M. T. Portes, E. Michard, P. Rosas-Santiago, M. A. Lizzio, C. O. Nunes, C. Campos, D. S. C. Damineli, J. C. Carvalho, P. T. Lima, O. Pantoja, J. A. Feijó, CORNICHON sorting and regulation of GLR channels underlie pollen tube $Ca2^+$ homeostasis. *Science* **360**, 533–536 (2018).

8. A. Alfieri, F. G. Doccula, R. Pederzoli, M. Grenzi, M. C. Bonza, L. Luoni, A. Candeo, N. R. Armada, A. Barbiroli, G. Valentini, T. R. Schneider, A. Bassi, M. Bolognesi, M. Nardini, A. Costa, The structural bases for agonist diversity in an *Arabidopsis thaliana* glutamate receptor-like channel. *Proc. Natl. Acad. Sci. U.S.A.* **117**, 752–760 (2020).

9. A. S. Raghavendra, V. K. Gonugunta, A. Christmann, E. Grill, ABA perception and signalling. *Trends Plant Sci.* **15**, 395–401 (2010).

10. F. Takahashi, T. Suzuki, Y. Osakabe, S. Betsuyaku, Y. Kondo, N. Dohmae, H. Fukuda, K. Yamaguchi-Shinozaki, K. Shinozaki, A small peptide modulates stomatal control via abscisic acid in long-distance signalling. *Nature* **556**, 235–238 (2018).

11. X. Zheng, S. Kang, Y. Jing, Z. Ren, L. Li, J.-M. Zhou, G. Berkowitz, J. Shi, A. Fu, W. Lan, F. Zhao, S. Luan, Danger-associated peptides close stomata by OST1-Independent activation of anion channels in guard cells. *Plant Cell* **30**, 1132–1146 (2018).

12. S. Gilroy, M. Białasek, N. Suzuki, M. Górecka, A. R. Devireddy, S. Karpiński, R. Mittler, ROS, calcium, and electric signals: Key mediators of rapid systemic signaling in plants. *Plant Physiol.* **171**, 1606–1615 (2016).

13. W. G. Choi, S. J. Swanson, S. Gilroy, High-resolution imaging of Ca^{2+}, redox status, ROS and pH using GFP biosensors. *Plant J.* **70**, 118–128 (2012).

14. E. E. Farmer, Y.-Q. Gao, G. Lenzoni, J.-L. Wolfender, Q. Wu, Wound- and mechanostimulated electrical signals control hormone responses. *New Phytol.* **227**, 1037–1050 (2020).

15. E. E. Farmer, D. Gasperini, I. F. Acosta, The squeeze cell hypothesis for the activation of jasmonate synthesis in response to wounding. *New Phytol.* **204**, 282–288 (2014).

16. M. Malone, Rapid, long-distance signal transmission in higher plants. *Adv. Bot. Res.* **22**, 163–228 (1996).

17. K. B. Hansen, F. Yi, R. E. Perszyk, H. Furukawa, L. P. Wollmuth, A. J. Gibb, S. F. Traynelis, Structure, function, and allosteric modulation of NMDA receptors. *J. Gen. Physiol.* **150**, 1081–1105 (2018).

18. E. S. Haswell, R. Peyronnet, H. Barbier-Brygoo, E. M. Meyerowitz, J.-M. Frachisse, Two MscS homologs provide mechanosensitive channel activities in the Arabidopsis root. *Curr. Biol.* **18**, 730–734 (2008).

19. S. A. R. Mousavi, C. T. Nguyen, E. E. Farmer, S. Kellenberger, Measuring surface potential changes on leaves. *Nat. Protoc.* **9**, 1997–2004 (2014).

20. G. Roblin, Analysis of the variation potential induced by wounding in plants. *Plant Cell Physiol.* **26**, 455–461 (1985).

21. D. Basu, E. S. Haswell, The mechanosensitive ion channel MSL10 potentiates responses to cell swelling in Arabidopsis seedlings. *Curr. Biol.* **30**, 2716–2728.e6 (2020).

22. G. Maksaev, E. S. Haswell, MscS-Like10 is a stretch-activated ion channel from *Arabidopsis thaliana* with a preference for anions. *Proc. Natl. Acad. Sci. U.S.A.* **109**, 19015–19020 (2012).

23. G. Maksaev, J. M. Shoots, S. Ohri, E. S. Haswell, Nonpolar residues in the presumptive pore-lining helix of mechanosensitive channel MSL10 influence channel behavior and establish a nonconducting function. *Plant Direct* **2**, e00059 (2018).

24. Y. Guerringue, S. Thomine, J.-M. Frachisse, Sensing and transducing forces in plants with MSL10 and DEK1 mechanosensors. *FEBS Lett.* **592**, 1968–1979 (2018).

25. E. S. Haswell, in *Current Topics in Membranes*, vol. 58 of *Mechanosensitive Ion Channels*, *Part A* (Academic Press, 2007), pp. 329–359.

26. N. Levina, S. Tötemeyer, N. R. Stokes, P. Louis, M. A. Jones, I. R. Booth, Protection of *Escherichia coli* cells against extreme turgor by activation of MscS and MscL mechanosensitive channels: Identification of genes required for MscS activity. *EMBO J.* **18**, 1730–1737 (1999).

27. C. D. Cox, N. Bavi, B. Martinac, Bacterial mechanosensors. *Annu. Rev. Physiol.* **80**, 71–93 (2018).

28. B. Reddy, N. Bavi, A. Lu, Y. Park, E. Perozo, Molecular basis of force-from-lipids gating in the mechanosensitive channel MscS. *eLife* **8**, e50486 (2019).

29. Y. Li, Y. Hu, J. Wang, X. Liu, W. Zhang, L. Sun, Structural insights into a plant mechanosensitive ion channel MSL1. *Cell Rep.* **30**, 4518–4527.e3 (2020).

30. Z. Deng, G. Maksaev, A. M. Schlegel, J. Zhang, M. Rau, J. A. J. Fitzpatrick, E. S. Haswell, P. Yuan, Structural mechanism for gating of a eukaryotic mechanosensitive channel of small conductance. *Nat. Commun.* **11**, 3690 (2020).

31. D. Basu, J. M. Shoots, E. S. Haswell, Interactions between the N- and C-termini of the mechanosensitive ion channel AtMSL10 are consistent with a three-step mechanism for activation. *J. Exp. Bot.* **71**, 4020–4032 (2020).

32. Y. Zou, S. Chintamanani, P. He, H. Fukushige, L. Yu, M. Shao, L. Zhu, D. F. Hildebrand, X. Tang, J.-M. Zhou, A gain-of-function mutation in *Msl10* triggers cell death and wound-induced hyperaccumulation of jasmonic acid in Arabidopsis. *J. Integr. Plant Biol.* **58**, 600–609 (2016).

33. Y. Nakayama, K. Yoshimura, H. Iida, Organellar mechanosensitive channels in fission yeast regulate the hypo-osmotic shock response. *Nat. Commun.* **3**, 1020 (2012).

34. H. R. Malcolm, J. A. Maurer, The mechanosensitive channel of small conductance (MscS) superfamily: Not just mechanosensitive channels anymore. *Chembiochem* **13**, 2037–2043 (2012).

35. C. T. Nguyen, A. Kurenda, S. Stolz, A. Chételat, E. E. Farmer, Identification of cell populations necessary for leaf-to-leaf electrical signaling in a wounded plant. *Proc. Natl. Acad. Sci. U.S.A.* **115**, 10178–10183 (2018).

36. K. Hashimoto, J. Murata, T. Konishi, I. Yabe, T. Nakamatsu, H. Kawasaki, Glutamate is excreted across the cytoplasmic membrane through the NCgl1221 channel of *Corynebacterium glutamicum* by passive diffusion. *Biosci. Biotechnol. Biochem.* **76**, 1422–1424 (2012).

37. J. Nakamura, S. Hirano, H. Ito, M. Wachi, Mutations of the *Corynebacterium glutamicum NCgl1221* gene, encoding a mechanosensitive channel homolog, induce L-glutamic acid production. *Appl. Environ. Microbiol.* **73**, 4491–4498 (2007).

38. Z. Qi, N. R. Stephens, E. P. Spalding, Calcium entry mediated by GLR3.3, an Arabidopsis glutamate receptor with a broad agonist profile. *Plant Physiol.* **142**, 963–971 (2006).

39. C. Ortiz-Ramírez, E. Michard, A. A. Simon, D. S. C. Damineli, M. Hernández-Coronado, J. D. Becker, J. A. Feijó, GLUTAMATE RECEPTOR-LIKE channels are essential for chemotaxis and reproduction in mosses. *Nature* **549**, 91–95 (2017).

40. C. Ast, J. Foret, L. M. Oltrogge, R. D. Michele, T. J. Kleist, C.-H. Ho, W. B. Frommer, Ratiometric Matryoshka biosensors from a nested cassette of green- and orange-emitting fluorescent proteins. *Nat. Commun.* **8**, 431 (2017).

41. M. L. Mayer, G. L. Westbrook, P. B. Guthrie, Voltage-dependent block by Mg^{2+} of NMDA responses in spinal cord neurones. *Nature* **309**, 261–263 (1984).

42. L. Nowak, P. Bregestovski, P. Ascher, A. Herbet, A. Prochiantz, Magnesium gates glutamate-activated channels in mouse central neurones. *Nature* **307**, 462–465 (1984).

43. C. Procko, S. E. Murthy, W. T. Keenan, S. A. R. Mousavi, T. Dabi, A. Coombs, E. Procko, L. Baird, A. Patapoutian, J. Chory, Stretch-activated ion channels identified in the touch-sensitive structures of carnivorous Droseraceae plants. *Elife* **10**, e64250 (2021).

44. M. J. Evans, R. J. Morris, Chemical agents transported by xylem mass flow propagate variation potentials. *Plant J.* **91**, 1029–1037 (2017).

45. U. Ricca, Transmission of stimuli in plants. *Nature* **117**, 654–655 (1926).

46. A. Kumari, A. Chételat, C. T. Nguyen, E. E. Farmer, Arabidopsis H$^+$-ATPase AHA1 controls slow wave potential duration and wound-response jasmonate pathway activation. *Proc. Natl. Acad. Sci. U.S.A.* **116**, 20226–20231 (2019).

47. K. Edwards, C. Johnstone, C. Thompson, A simple and rapid method for the preparation of plant genomic DNA for PCR analysis. *Nucleic Acids Res.* **19**, 1349 (1991).

48. T. A. Enders, S. Oh, Z. Yang, B. L. Montgomery, L. C. Strader, Genome sequencing of Arabidopsis *abp1-5* reveals second-site mutations that may affect phenotypes. *Plant Cell* **27**, 1820–1826 (2015).

49. M. Sturm, C. Schroeder, P. Bauer, SeqPurge: Highly-sensitive adapter trimming for paired-end NGS data. *BMC Bioinformatics* **17**, 208 (2016).

50. H. Li, B. Handsaker, A. Wysoker, T. Fennell, J. Ruan, N. Homer, G. Marth, G. Abecasis, R. Durbin, The sequence alignment/map format and SAMtools. *Bioinformatics* **25**, 2078–2079 (2009).

51. W. Shen, S. Le, Y. Li, F. Hu, SeqKit: A cross-platform and ultrafast toolkit for FASTA/Q file manipulation. *PLOS ONE* **11**, e0163962 (2016).

52. J. Schindelin, I. Arganda-Carreras, E. Frise, V. Kaynig, M. Longair, T. Pietzsch, S. Preibisch, C. Rueden, S. Saalfeld, B. Schmid, J. Y. Tinevez, D. J. White, V. Hartenstein, K. Eliceiri, P. Tomancak, A. Cardona, Fiji: An open-source platform for biological-image analysis. *Nat. Methods* **9**, 676–682 (2012).

53. G. Maksaev, E. S. Haswell, Expression and characterization of the bacterial mechanosensitive channel MscS in *Xenopus laevis* oocytes. *J. Gen. Physiol.* **138**, 641–649 (2011).

54. F. Lemoine, D. Correia, V. Lefort, O. Doppelt-Azeroual, F. Mareuil, S. Cohen-Boulakia, O. Gascuel, NGPhylogeny.fr: New generation phylogenetic services for non-specialists. *Nucleic Acids Res.* **47**, W260–W265 (2019).

55. I. Letunic, P. Bork, Interactive Tree Of Life (iTOL) v4: Recent updates and new developments. *Nucleic Acids Res.* **47**, W256–W259 (2019).

56. K. Katoh, J. Rozewicki, K. D. Yamada, MAFFT online service: Multiple sequence alignment, interactive sequence choice and visualization. *Brief. Bioinform.* **20**, 1160–1166 (2019).

57. K. Katoh, K. Kuma, H. Toh, T. Miyata, MAFFT version 5: Improvement in accuracy of multiple sequence alignment. *Nucleic Acids Res.* **33**, 511–518 (2005).

58. B. J. Grant, A. P. C. Rodrigues, K. M. ElSawy, J. A. McCammon, L. S. D. Caves, Bio3d: An R package for the comparative analysis of protein structures. *Bioinformatics* **22**, 2695–2696 (2006).

59. L. Skjærven, X.-Q. Yao, G. Scarabelli, B. J. Grant, Integrating protein structural dynamics and evolutionary analysis with Bio3D. *BMC Bioinformatics* **15**, 399 (2014).

60. E. de Castro, C. J. A. Sigrist, A. Gattiker, V. Bulliard, P. S. Langendijk-Genevaux, E. Gasteiger, A. Bairoch, N. Hulo, ScanProsite: Detection of PROSITE signature matches and ProRule-associated functional and structural residues in proteins. *Nucleic Acids Res.* **34**, W362–W365 (2006).

61. C. J. A. Sigrist, L. Cerutti, E. de Castro, P. S. Langendijk-Genevaux, V. Bulliard, A. Bairoch, N. Hulo, PROSITE, a protein domain database for functional characterization and annotation. *Nucleic Acids Res.* **38**, D161–D166 (2010).

62. Y. Zhou, W. Yang, M. Kirberger, H.-W. Lee, G. Ayalasomayajula, J. J. Yang, Prediction of EF-hand calcium-binding proteins and analysis of bacterial EF-hand proteins. *Proteins* **65**, 643–655 (2006).

63. A. Waterhouse, M. Bertoni, S. Bienert, G. Studer, G. Tauriello, R. Gumienny, F. T. Heer, T. A. P. de Beer, C. Rempfer, L. Bordoli, R. Lepore, T. Schwede, SWISS-MODEL: Homology modelling of protein structures and complexes. *Nucleic Acids Res.* **46**, W296–W303 (2018).

64. S. Wang, S. Sun, Z. Li, R. Zhang, J. Xu, Accurate *de novo* prediction of protein contact map by ultra-deep learning model. *PLOS Comput. Biol.* **13**, e1005324 (2017).

65. C. Magnan, P. Baldi, SSpro/ACCpro 5: Almost perfect prediction of protein secondary structure and relative solvent accessibility using profiles, machine learning and structural similarity. *Bioinformatics* **30**, 2592–2597 (2014).

66. B. Adhikari, J. Cheng, CONFOLD2: Improved contact-driven ab initio protein structure modeling. *BMC Bioinformatics* **19**, 22 (2018).

67. B. Webb, A. Sali, Comparative protein structure modeling using MODELLER, *Curr. Protoc. Bioinformatics* **54**, 5.6.1–5.6.37 (2016).

68. T. Nugent, D. T. Jones, Membrane protein orientation and refinement using a knowledge-based statistical potential. *BMC Bioinformatics* **14**, 276 (2013).

69. R. F. Alford, J. K. Leman, B. D. Weitzner, A. M. Duran, D. C. Tilley, A. Elazar, J. J. Gray, An integrated framework advancing membrane protein Modeling and design. *PLOS Comput. Biol.* **11**, e1004398 (2015).

70. R. F. Alford, P. J. Fleming, K. G. Fleming, J. J. Gray, Protein structure prediction and design in a biologically realistic implicit membrane. *Biophys. J.* **118**, 2042–2055 (2020).

71. M. Michel, D. Menéndez Hurtado, K. Uziela, A. Elofsson, Large-scale structure prediction by improved contact predictions and model quality assessment. *Bioinformatics* **33**, i23–i29 (2017).

72. W. G. Choi, M. Toyota, S.-H. Kim, R. Hilleary, S. Gilroy, Salt stress-induced Ca^{2+} waves are associated with rapid, long-distance root-to-shoot signaling in plants. *Proc. Natl. Acad. Sci. U.S.A.* **111**, 6497–6502 (2014).

73. J. Choi, K. Tanaka, Y. Cao, Y. Qi, J. Qiu, Y. Liang, S. Y. Lee, G. Stacey, Identification of a plant receptor for extracellular ATP. *Science* **343**, 290–294 (2014).

74. S. S. Scholz, J. Malabarba, M. Reichelt, M. Heyer, F. Ludewig, A. Mithöfer, Evidence for GABA-induced systemic GABA accumulation in Arabidopsis upon wounding. *Front. Plant Sci.* **8**, 388 (2017).

75. E. Krol, T. Mentzel, D. Chinchilla, T. Boller, G. Felix, B. Kemmerling, S. Postel, M. Arents, E. Jeworutzki, K. A. S. Al-Rasheid, D. Becker, R. Hedrich, Perception of the Arabidopsis danger signal peptide 1 involves the pattern recognition receptor *At*PEPR1 and its close homologue *At*PEPR2. *J. Biol. Chem.* **285**, 13471–13479 (2010).

76. X. Zheng, K. He, T. Kleist, F. Chen, S. Luan, Anion channel SLAH3 functions in nitrate-dependent alleviation of ammonium toxicity in Arabidopsis. *Plant Cell Environ.* **38**, 474–486 (2015).